

A facile and controllable electrochemically fabricated nonstoichiometric MoO_x film for novel opto-electronic devices

Ranran Zeng¹, Hong Liu^{1,3}  and Wenzhong Shen^{1,2,3}

¹ Institute of Solar Energy, and Key Laboratory of Artificial Structures and Quantum Control (Ministry of Education), School of Physics and Astronomy, Shanghai Jiao Tong University, Shanghai 200240, People's Republic of China

² Collaborative Innovation Center of Advanced Microstructures, Nanjing 210093, People's Republic of China

E-mail: liuhong@sjtu.edu.cn and wzshen@sjtu.edu.cn

Received 16 October 2018, revised 5 March 2019

Accepted for publication 8 March 2019


Published 7 May 2019



Abstract

Non-stoichiometric transition metal oxides have received considerable attention because of their excellent optical and electrical properties for novel high performance opto-electronic devices or photocatalysis, among which MoO_x was one promising candidate. However, few studies have been focused on its evolution under different controlling parameters and ambient conditions. In this work, we report a facile electrochemical method for smooth and uniform non-stoichiometric MoO_x films, with effective control of the morphology, chemical composition and microstructure of molybdenum simply by a few physical/chemical parameters. The modification of roughness, crystallinity, oxygen vacancy concentration can play an important role in their opto-electronic performances, e.g. in the perovskite solar cells. As a result, a conversion efficiency of 9.20% could be obtained by control of oxygen vacancies and crystallinity and could be further improved with the change of transparencies. Furthermore, its wetting properties could be significantly influenced for further applications, especially for fabrication of novel detectors and perovskite solar cells.

Keywords: nonstoichiometric materials, metal oxide, electrochemical fabrication, structural and content evolution, physical and chemical manipulation

 Supplementary material for this article is available [online](#)

(Some figures may appear in colour only in the online journal)

1. Introduction

In recent years, non-stoichiometric metal oxides such as NiO_x [1, 2], CuO_x [3, 4], WO_x [5], MoO_x [5, 6], and TiO_x [7–9] have drawn great interest due to their excellent properties (tunable wide band gap, high electron/hole transportability, photo/electrochromic effect and so forth) toward novel optical, electrical and photocatalytic devices with high stability and low cost. In particular, MoO_x is one promising candidate for hole transport layer (HTL) in perovskite solar cells (PSCs) owing to its

non-toxicity, large band gap and deep electronic state [10, 11]. Xiao *et al* applied MoO_x as HTL in p-i-n type PSC with efficiency of 5.9% [6]. Tseng *et al* treated MoO_x with UV-ozone to improve the surface coverage of the perovskite layer and achieved the efficiency of 13.1% [5]. Moreover, MoO_x has also received considerable attention for research and development in a variety of applications, such as photochromic and electrochromic [12–16], gas sensors [17–19], photocatalytic [20], lithium ion batteries [21] and light emitting diodes [22].

According to a previous report [23], amorphous MoO_x film is quite a susceptible material, which means the non-uniformity and time evolution of its stoichiometry and

³ Authors to whom any correspondence should be addressed.

microstructure have been quite significant. This could be an essential issue both in its fabrication and in its performance in devices as a stable element. Up till now, only a few studies have been carried out for the correlation between some properties and the annealing conditions and its consequence, however more systematic investigations concerning such issues under composite conditions are yet to be carried out [24–28]. The aforementioned molybdenum oxide films were all prepared via thermal evaporation in vacuum, which has significant drawbacks in cost and scalability for large area samples. Meanwhile, various chemical synthesis methods in liquid phase have also been developed, such as sol-gel [29], spray pyrolysis [30], and spin coating [11], which are significantly more simple. In those methods, the motion of reactive species only relies on thermal diffusions that could influence the quality of the formation of layers on substrates. To amend that, electrochemical deposition appears to be the more likely promising candidate as a cheap and controllable technique that could provide effective control of morphology, composition as well other properties of the deposit at room temperature under ambient conditions [31–34]. In addition, it also enables large-area film preparation without any mechanical instruments [1, 35].

In this work, we report a facile electrochemical method for non-stoichiometric metal oxide films with studies of evolution of its physical and chemical properties with various parameters. A smooth and uniform MoO_x could be easily formed using cyclic voltammetry (CV) method. Its stoichiometry, crystallinity and morphology could be effectively controlled by experimental parameters and ambient conditions (UV illumination, annealing time, temperature and atmosphere) so as to achieve different physical properties for corresponding applications in solar cells and other devices [25]. As a result, the p-i-n type PSCs employing the electrochemically deposited MoO_x as HTL can achieve a power conversion efficiency (PCE) up to 9.20% which could be further raised by improvements such as the transparency of light incident side. Furthermore, it has also been found that the wetting property of this MoO_x could be significantly influenced by those conditions, which would be important for its further applications, especially for detectors and improvement for the fabrication of stable PSCs.

2. Experimental

2.1. Synthesis and modification of MoO_x

Firstly, 0.34 M aqueous solution of hexaammonium molybdate $(\text{NH}_4)_6\text{Mo}_7\text{O}_{24}$, 99% Energy Chemical) was prepared with deionized water, and then slowly mixed with 20 ml ethylene glycol (99% Sinopharm). The solution was stirred for 20 min at the rate of 50 to 150 rpm. The FTO-coated glass substrates ($15 \Omega \text{ sq}^{-1}$, Materwin) were sequentially cleaned by ultrasonic bath in detergent, deionized water, acetone, isopropanol and ethanol for 15 min in each step. These cleaned FTO substrates were exposed to UV-ozone treatment for 20 min. The electrodeposition of MoO_x was performed on an FTO-coated glass substrate using a standard three-electrode

electrochemical system with the FTO substrate as the working electrode (WE), Ag/AgCl (3 M KCl) as the reference electrode (RE) and platinum foil as the counter electrode (CE). The electrodeposition was controlled by an electrochemical workstation (CS350, Corrtest) at room temperature in cyclic voltammetry (CV) mode, using lower and upper potential limits of -1.2 to -0.8 V and -0.5 to 1.0 V, respectively, with the number of cycles from 1 to 5. After the deposition, the films were washed with deionized water. The annealing was carried out in a vacuum crucible furnace (VBF-1200X-H8, Hefei Kejing) under different chemical atmospheres. After the post-treatments (UV-ozone and annealing under different chemical atmospheres), the substrates were transferred quickly into a nitrogen-filled glovebox.

2.2. Characterization of MoO_x

A field emission scanning electron microscope (FE-SEM, Zeiss Ultra Plus) was applied to observe the surface morphology and thickness of the MoO_x films on the FTO-coated glass substrates. The chemical state of the samples was analyzed by x-ray photoelectron spectroscopy (XPS, AXIS Ultra DLD). The XPS spectra were fitted with the Gaussian–Lorentzian product using the XPSPEAK41 software package. Their microstructure was detected by grazing incidence x-ray diffraction (GIXRD), at the 7.3.3 beamline (10 keV) at advanced light source (ALS) of Lawrence Berkeley National Laboratory (LBNL). The scattering intensity was detected by a PILATUS 2M detector and a two-dimensional (2D) area detector was employed here to obtain more complete crystal information than the diffraction intensity versus 2θ plot. The transmission spectra of the thin film samples were measured by ultraviolet/visible/near-infrared (UV/VIS/NIR) Spectrophotometer (Lambda 950, PerkinElmer). The surface roughness of the films was characterized by an atomic force microscope (AFM, Innova). The contact angles of water droplets were measured on a contact angle measuring system (DSA100, KRÜSS) at room temperature.

2.3. Assembling PSCs based on MoO_x

The fabrication of the perovskite layer was performed in a N_2 protected glove box. 1.45 M PbI_2 (99% Sigma-Aldrich) and equimolar MAI (99.5% Materwin) were dissolved in a 7:3 (v/v) mixture of γ -butyrolactone (GBL, 99.9% Aladdin) and dimethyl sulfoxide (DMSO, 99.9% Aladdin) by stirring overnight at 60°C . The perovskite precursor solution was spin-coated onto the MoO_x film at 1000 rpm for 12 s and then at 4000 rpm for 30 s, during which 150 ml toluene was continuously dripped onto the spinning film. The sample was then annealed at 100°C for 10 min. After cooling down, the [6,6]-phenyl C₆₁ butyric acid methyl ester (PC_{61}BM , 99% Xi'an Polymer Light Technology Corp.) film was then deposited on the as-formed samples by spin-coating a chlorobenzene solution of PC_{61}BM (20 mg ml^{-1}) at 2000 rpm for 60 s and desiccation at 70°C for 10 min. Afterwards, a bathocuproine (BCP, 99% Xi'an Polymer Light Technology Corp.) layer was sequentially deposited on the PC_{61}BM layer by spin-coating

an isopropanol solution of BCP (0.5 mg ml^{-1}) at 500 rpm for 5 s and then at 4000 rpm for 30 s, followed by desiccation at 70°C for 10 min. Finally, a 120 nm-thick Ag was thermally evaporated on top of the BCP layer of the electrode. The active area of the device is 0.25 cm^2 .

2.4. Characterization of solar cells

The steady-state photoluminescence (PL) was measured by a Raman spectrometer (LABRAM HR800, Horiba Jobin Yvon system (France)) with excitation at 514.5 nm by an argon ion laser. For the PSC devices, the current density–voltage (J – V) characteristics were measured using a standard Solar Simulator (Newport, Oriel Sol-2A) under 1 sun AM 1.5 illumination. The simulator was calibrated by a standard reference Si solar cell (effective area $2 \times 2 \text{ cm}^2$, certified by VLSI Standards Inc.) before the measurement. All J – V curves were scanned from -0.5 V to 1.5 V . The scanning rate and time delay were 0.15 V s^{-1} and 10 ms, respectively. The external quantum efficiency (EQE) spectra were recorded by a quantum efficiency/IPCE system (PV Measurements Inc., QEX10) in 300–850 nm wavelength range in air.

3. Results and discussion

In conventional electrochemical deposition of metal oxides, experiments are normally carried out in acidic or alkaline electrolytes, for which a good control of the pH value becomes necessary and needs to be successively controlled by titration method throughout the process. In this work, we carried out the fabrication in hexaammonium molybdate solution and no titration was needed. For higher quality of film growth, the CV method has been applied and investigated [1, 33, 36, 37]. Figure 1(a) shows corresponding I – V curves recorded at the sweep rate of 3 mV s^{-1} , 5 mV s^{-1} , and 10 mV s^{-1} , respectively. The curves are almost coincident at the rate of 3 mV s^{-1} and 10 mV s^{-1} , but the peak of the negative cycle becomes stronger at 5 mV s^{-1} . As shown in figures 1(b)–(d), the film thickness gradually decreases as the cycle rate increases. However, at 10 mV s^{-1} , the as-deposited film could not completely cover the FTO-coated glass substrate in figure 1(d). Therefore, the sweep rate of 5 mV s^{-1} appeared to be a more suitable condition for deposition. Moreover, we have investigated the influence of the lower limit of the potential on the morphology of the electrodeposited film. The CV experiments were then carried out using a series of lower potential limits of -1.2 , -1.0 and -0.8 V . As shown in figure 1(f), when the lower limit potential was -0.8 V , the reduction current was very low and the film could not completely cover the substrate. The film became uniform for the lower limit at -1.0 and -1.2 V and increased with the value of lower limit potential. At -1.2 V in figure 1(h), the film was too thick, which could eventually lead to high series resistance and lower transparencies [38]. Therefore, the moderate condition (-1.0 to 0.5 V at 5 mV s^{-1} for 1 cycle) appears more suitable for p-i-n PSCs in which MoO_x acts as both HTL and light incident side. The higher

lower limit in CV method could be used in other fields such as the photocatalysis, where a longer light path would be more important and serial resistance becomes less important.

To qualitatively determine the formation of MoO_x , XPS measurements have been carried out to confirm the stoichiometric composition of the virgin film, in which 284.8 eV of C1s orbit has been chosen as the reference binding energy. First of all, the full spectrum in figure 1(i) shows the peaks of Mo3s, Mo3d, Mo3p, Mo4s, C1s and O1s. Secondly, the high resolution XPS spectrum of Mo3d core level peaks is exhibited in figure 1(j). The Mo3d spectrum can be divided into one 3d doublet in the form of Gaussian function, corresponding to the oxidation state of Mo. The fitting peaks located at 235.2 eV and 231.9 eV are assigned to the Mo^{5+} valence state [32, 39], then the O1s spectrum is shown in figure 1(k). According to previous studies, it is known that the peak at $\sim 530 \text{ eV}$ is due to the oxide, the one at $\sim 532 \text{ eV}$ is attributed to oxygen species dissolved in the metal or adsorbed oxygen (such as O^- , OH^- , or H_2O) [40]. This result represents the significant existence of molybdenum Mo^{5+} valence state in the as-fabricated sample. Taking into account the previous characterization, it can be confirmed that the as-deposited sample was non-stoichiometric MoO_x ($x = 2.5$).

In the many applications of non-stoichiometric metal oxides, their crystallinity and stoichiometry have always been important factors that determine its performance in gas sensors, photocatalysis, and photochromic/electrochromic devices and so forth [12–14, 18]. As commonly known, amorphous MoO_x film is quite susceptible to ambient conditions [23]. Therefore, we have systematically studied the effects of these conditions (UV-ozone, temperature, time and atmosphere) on the MoO_x film. To investigate the crystallinity of the sample fabricated, we have applied 2D GIXRD (incident x-ray angle at 0.3°) for the FTO substrate (figure 2(a)), the thin MoO_x film obtained (figure 2(b)) and the MoO_x films after different post-treatments (figures 2(c)–(f)). Figures 2(a) and (b) indicate that the as-deposited film was amorphous because no significant diffraction peak of MoO_x was detected during $q = 0.5$ – 4.0 \AA^{-1} . The results with UV-ozone (figure 2(c)) show no other significant diffraction peak compared to figure 2(a), indicating that the corresponding films were still amorphous. However, more diffraction peaks can be observed in figures 2(d) and (e), for samples annealed in air and oxygen, respectively. In figure 2(d), there were broad diffraction peaks related to the (002), (040) and (060) crystal planes, while the one related to (020) plane was quite sharp and intense. Since the (020) plane is located close to the q_z axis, it indicates that the grains in the MoO_x film annealed in air had their face-on orientation parallel to the surface of the film. As for the case of O_2 , there was observed four diffraction peaks along the Debye rings, with their intensity stronger than that in figure 2(d), especially the ones at the (020) and (060) directions. Surprisingly, for the sample annealed in nitrogen (figure 2(f)), there was no significant additional diffraction peak discovered, which means quite weak crystallization in the MoO_x annealed in N_2 . The average grain size of MoO_x can be obtained from the

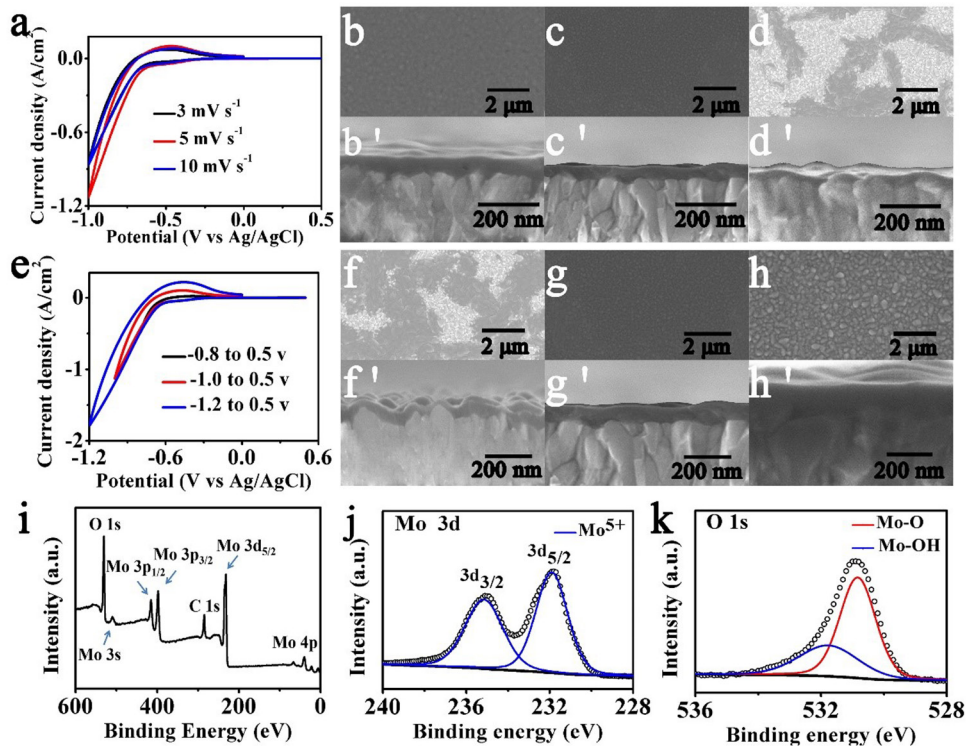


Figure 1. MoO_x fabricated under different electrochemical conditions: (a) cyclic voltammetry curves with different sweep rate; (b)–(d) top view and (b')–(d') cross-sectional SEM images of the deposits at: (b) and (b') 3 mV s^{−1}; (c) and (c'), 5 mV s^{−1}; (d) and (d') 10 mV s^{−1}; (e) cyclic voltammetry curves with different lower potential limit; (f)–(h) top view and (f')–(h') cross-sectional SEM images of the deposits with the lower limit at: (f) and (f') −0.8 V; (g) and (g') −1.0 V; (h) and (h') −1.2 V; (i)–(k) XPS spectra of the deposits: (i) full spectrum; (j) Mo3d; (k) O1s.

Debye-Scherrer equation of $D = 0.89\lambda/(\beta \cos \theta)$, where β is the half-width of the diffraction peak, λ is the wavelength of the x-ray and θ is the diffraction angle [41]. The β for the samples annealed in air and oxygen atmospheres are 0.0037 and 0.0025 rad, respectively. Therefore the average crystalline sizes for MoO_x annealed in air and oxygen are around 37 and 55 nm, respectively. According to the experimental observations of Andreas *et al*, peaks at 12.76°, 25.70°, and 38.98° indicate formation of α -MoO₃, consistent with the positions shown in figure S4 in the supplementary information (stacks.iop.org/JMM/29/065012/mmedia) [42].

The stoichiometry of the post-treated samples was characterized by high resolution XPS, as shown in figure 3. The Mo3d spectra contained only one 3d doublet located at 236.3 eV, 233.2 eV (figure 3(a)), 236.0 eV, 232.8 eV (figure 3(b)), and 236.3 eV, 233.2 eV (figure 3(c)) that are all related to Mo⁶⁺ [39, 43]. The MoO_x has seemingly completely turned into MoO₃ by UV-ozone and annealing processes in air or O₂, with the Mo⁵⁺ all being oxidized to Mo⁶⁺. For the MoO_x film annealed in nitrogen atmosphere, there are two 3d doublets in the form of a Gaussian function as shown in figure 3(d). The ones centered at 236 eV and 232.8 eV are the typical doublet of Mo⁶⁺, while the other ones centered at 234.6 eV and 231.9 eV are the typical doublet of Mo⁵⁺ [31, 43]. Assuming the ratio of the quantity of Mo⁵⁺/Mo⁶⁺ (calculated from the ratio of integrated peak area) is k , it can be easily calculated that $x = 2.5 + (2k + 2)^{-1}$. In this situation, the ratio of Mo⁵⁺/Mo⁶⁺ is 0.77, which means $x = 2.78$.

Beside direct characterizations, it is important to study opto-electronic properties of the MoO_x samples before being integrated with different materials in devices. Firstly, the UV–vis transmission spectra of various MoO_x films have been studied and illustrated in figure 3(e). It is clearly observed that the untreated film has shown quite high transparency in the region from 350 to 800 nm, which is important to avoid the parasitic absorption loss of perovskite. When the molybdenum oxide films were subjected to different post-treatments, the transmittance shows no substantial change. However, the transmittance of the film annealed in a nitrogen atmosphere was lower (figure S3). Such a change might be attributed to the content of oxygen vacancies in the films, according to some previous report [13]. Furthermore, we can deduce the bandgap information from the transmittance measurement. According to Lee *et al*, MoO₃ is a wide, indirect bandgap semiconductor [26]. The optical band-gap (E_g) of the samples can be calculated from the equation $\alpha h\nu = A(h\nu - E_g)^{1/2}$ [43], where A is the proportionality constant, α is the absorption coefficient and $h\nu$ is the photon energy. As shown in figure 3(f), taking $h\nu$ as the horizontal axis and $\alpha h\nu$ as the vertical axis, E_g can be estimated by extrapolating the linear portion of the curve to zero absorption. The E_g of the MoO_x films was estimated to be 3.31 eV, 3.90 eV, 3.89 eV, 3.88 eV and 3.85 eV for the samples unprocessed, treated with UV-ozone, annealed in air, O₂ and N₂, respectively. In general, the E_g of the post-treated films were all significantly larger than the original one. Such increase of E_g may be due

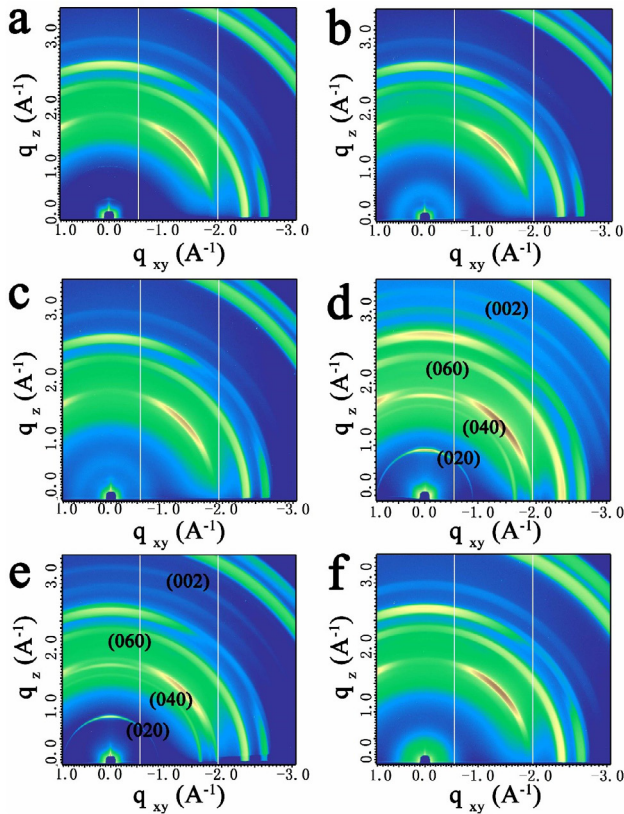


Figure 2. 2D-GIXRD patterns for different samples: (a) The FTO substrate, (b) MoO_x film deposited on FTO, and MoO_x films treated under different conditions: (c) UV-ozone, 20 min; (d) annealing in air at 300 °C, 120 min; (e) annealing in O₂ at 300 °C, 120 min; (f) annealing in N₂ at 300 °C, 120 min.

to the decrease of oxygen vacancies that could restrain excess electron generation [27, 28].

To investigate the application of the electrochemical MoO_x films in real devices, we have attempted to apply these MoO_x in the p-i-n type planar hybrid PSCs based on the structure of FTO/MoO_x/MAPbI₃/PC₆₁BM/BCP/Ag. Figure 4(a) shows the top-view SEM image of the perovskite film deposited on MoO_x film. The MAPbI₃ film exhibits a homogeneous and pin-hole free morphology and large grain size, which were propitious to reduce the electron-hole recombination. PL measurements were performed to investigate charge carrier extraction capability of the MoO_x with different post-processing. As shown in figure 4(b), the peaks centered at 754, 741, 775, 772, 762 nm are corresponding to samples untreated, treated by UV-ozone, annealed in air, oxygen, and nitrogen, respectively. There was a redshift for the annealed samples, which could possibly be attributed to the crystallization in the MoO_x films. Moreover, the annealing atmosphere has also affected the intensity of this feature. The samples treated in oxygen atmosphere show the most intense peak intensity, while the ones treated in air show significantly weaker peaks. The lowest PL intensity was found for MoO_x films annealed in nitrogen atmosphere. The MoO_x films annealed in nitrogen atmosphere exhibited more efficient PL quenching, which could be advantageous for the function of HTLs in PSCs. Noticeably, the N₂ annealed samples have the smallest redshift of PL peak, indicating a

lower level of crystallization than the sample annealed under O₂, which was to some degree related to the previous GIXRD measurement.

The configuration of the entire PSC device is illustrated in figure 4(c), with a 35 nm thick MoO_x, 300 nm thick perovskite, 80 nm thick PC₆₁BM/BCP and 120 nm thick silver electrode. The *J*-*V* curves of the best solar cells are shown in the same figure (detailed photovoltaic characteristics can be found in table S1). Apparently, the performance of the solar cells is strongly dependent on different post-treatments of the MoO_x HTL. The assembled p-i-n PSC with untreated MoO_x HTL shows quite low performance, with a poor efficiency of only 0.04%, with *V*_{OC} = 0.34 V, *J*_{SC} = 0.78 mA cm⁻² and FF = 0.16. The devices based on air annealing MoO_x film obtain a PCE of 1.06% with *V*_{OC} = 0.82 V, *J*_{SC} = 2.52 mA cm⁻² and FF = 0.51, while for the MoO_x film annealing in O₂, the values are *η* = 1.92% with *V*_{OC} = 0.70 V, *J*_{SC} = 5.47 mA cm⁻² and FF = 0.49. Noticeably, the highest efficiency of 4.49% (with *V*_{OC} = 0.94 V, *J*_{SC} = 7.77 mA cm⁻², FF = 0.61) was achieved under N₂ atmosphere. The presence of oxygen vacancies plays a key role in generating positively charged structural defects in the band gap and transporting carriers, and compared to the stoichiometric MoO₃, the devices using non-stoichiometric MoO_x display a good performance [26, 44]. In the meantime, too high oxygen vacancy concentration might also be a problem due to possible semiconductor-metal transition, and eventually lead to device failure [26]. According to this, the main origin for the distinctive performance of PSCs by annealing with N₂ and O₂ atmosphere is the amount of oxygen vacancies and complete absence of oxygen vacancies (according to previous calculation for figure 3) under these two conditions, respectively. The annealing under air atmosphere can generate a smaller quantity of oxygen vacancies than that under O₂ atmosphere (though it may not be significantly detected in XPS due to its sensitivity limitation), which has induced higher performance of PSCs. More interestingly, combining both the PL and GIXRD results, it can be seen that the highest performance in PSCs was with the lowest level of crystallization by annealing with N₂. Work from other researchers have reported good performance of cells with amorphous substrate as well [11]. Nevertheless, the mechanism of this phenomenon—why less crystallinity and better performance manifests under N₂—still needs further investigation, for example theoretical calculations.

The influence of temperature and time on the PSCs was studied further with nitrogen atmosphere annealing toward better optimization for the device performance, as shown in figure 4(d) (detailed performance data can be found in table S2). For the temperature, *V*_{OC}, *J*_{SC}, FF and PCE were all significantly increased with the increasing of the annealing temperature from 250 °C to 300 °C. However, when the temperature was higher than 300 °C, the efficiency began to significantly decrease with a considerable decrease of the *R*_{sh}, which could be due to the great enhancement of inhomogeneity of the film under such a high temperature (can be referred from the SEM image in figure S5(a)). The PCE gradually increased with the annealing time increasing from 60 min to 210 min, and then began to decrease after 210 min,

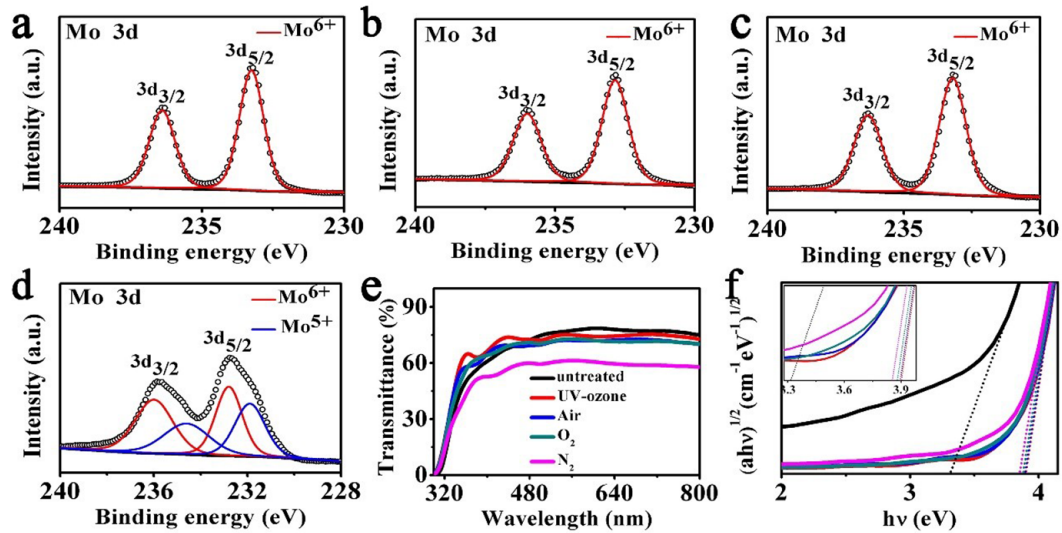


Figure 3. Chemical and optical characterization of MoO_x under different conditions: (a) UV-ozone, 20 min; (b) annealing in air at 300 °C, 120 min; (c) annealing in O_2 at 300 °C, 120 min; (d) annealing in N_2 at 300 °C, 120 min; (e) the transmittance of the MoO_x films treated under different conditions; (f) Tauc plots of MoO_x films for calculation of E_g .

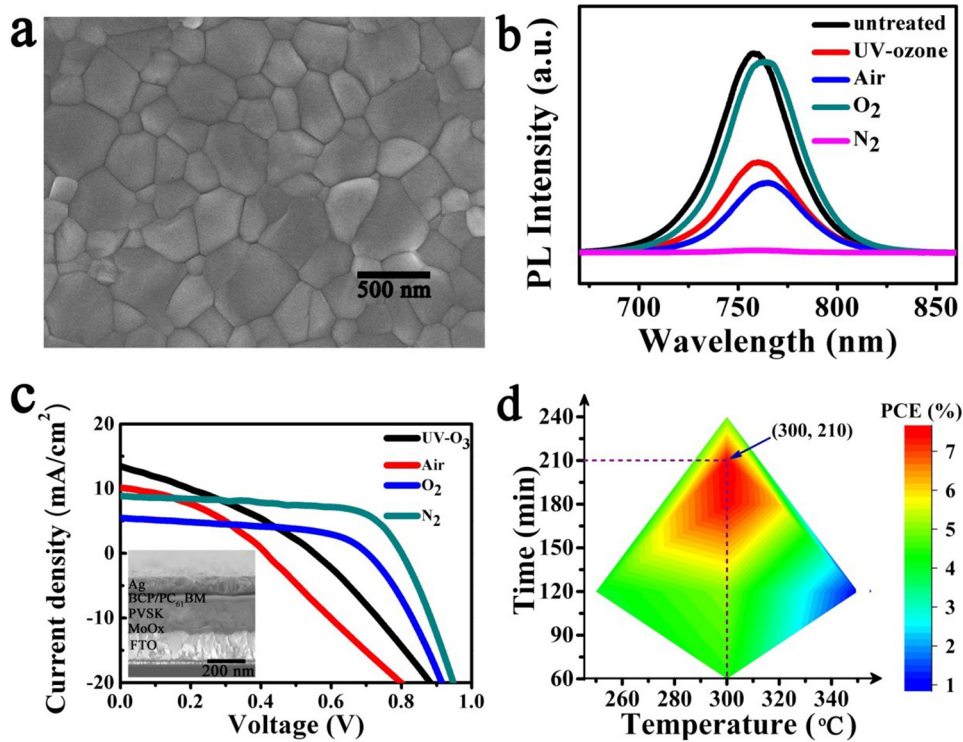


Figure 4. Characteristics of perovskite solar cells: (a) top-view SEM image of the perovskite film deposited on MoO_x film; (b) PL of samples under different conditions; (c) J - V curves of the PSCs with MoO_x HTL under different conditions, with the inset showing the cross-sectional view of the cell structure; (d) efficiency profile of different annealing temperatures and times in a nitrogen atmosphere.

which could also be due to the inhomogeneity of the film as shown in figure S5(b). Therefore, as shown in figure 4(d), conditions around 300 °C and 210 min would be more suitable for a better performance of the MoO_x in the PSCs.

Up till now, the performance of the MoO_x in PSCs appeared to be low compared to previous methods. According to the principle of the reaction, bubbles of hydrogen can be generated during the electrochemical reactions, so mechanical stirring is another favorable factor for further

optimization [45]. Hence, we have carried out the fabrication with different mechanical stirring rates using the optimized annealing condition. As indicated in figure 5, the performance of the PSCs was significantly improved by the application of stirring. The PCE reached 7.70% (with $V_{OC} = 0.89$ V, $J_{SC} = 12.04$ mA cm^{-2} and $FF = 0.72$) at 50rpm and became gradually higher at 100rpm ($\eta = 9.20\%$, $V_{OC} = 0.91$ V, $J_{SC} = 14.27$ mA cm^{-2} , and $FF = 0.71$). As the stirring speed was further increased to 150rpm, the device performance

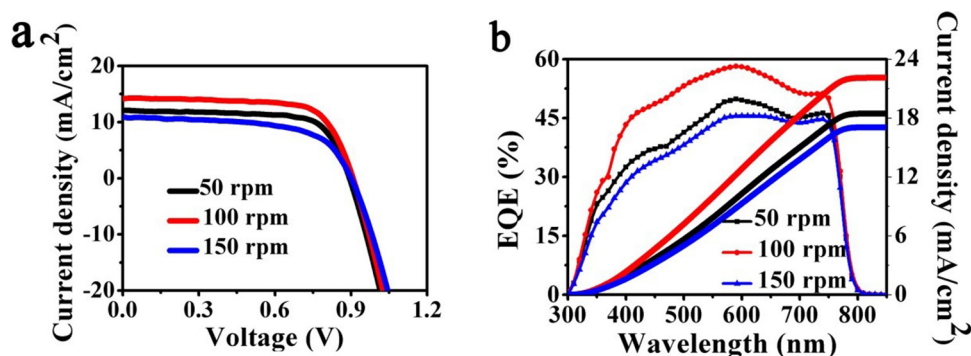


Figure 5. Effect of mechanical stirring on the performance of MoO_x in PSCs: (a) *J*–*V* curves of the optimized perovskite solar cells with MoO_x HTL at different stirring rate; (b) corresponding EQE of the optimized perovskite solar cells.

began to slightly decrease, which indicated that too high a stirring rate might influence the ionic current so that the stability of deposition deteriorates. The corresponding EQE spectra are shown in figure 5(b), including the integrated current densities as a function of wavelength. All the devices have exhibited a strong response in a broad range from 400 to 750 nm, and the EQE of the sample at 100 rpm exceeded other devices within the entire region. In addition, the *J*_{SC} values calculated from the EQE curves were 18.47, 22.11 and 17.07 mA cm^{−2} at stirring rates of 50, 100 and 150 rpm, respectively, which is consistent with the variation of the *J*–*V* curve. As can be observed, the FF was significantly improved, which means the quite good conductivity of the as-fabricated MoO_x film, which is also important for its application in devices other than solar cells. The main reason why the efficiency of those cells was still lower than the commonly known PSCs is most likely due to the low transparency of the electrochemically fabricated MoO_x (as can be seen in figure S3). Nevertheless, the electrochemically fabricated MoO_x has shown significant feasibility and facile controllability for devices in practice, yet can still be improved by the enhancement of transparency by doping when being adapted for optical components.

According to above results and previous reports, MoO_x has been quite susceptible to ambient conditions, and as widely recognized in practice, the combination of the layer with other materials has always been important for real devices. Therefore, it will also be important to study any macroscopic changes of the surface situation that could be induced by previous experiments. We have therefore carried out measurement of the contact angles of the samples under different conditions. As shown in figure 6, significant changes have taken place after the treatments. In general, all the contact angles have been reduced after annealing. Among those results, the final contact angle was the lowest in air, a mixture of N₂ and O₂, and highest in pure N₂. Such variation could be due to the composite effect of oxygen vacancies and morphology change due to nucleation [46, 47]. On the one hand, the formation of oxygen vacancies can result in lattice relaxation and a decrease of surface tension, which explains the relatively higher contact angle under N₂ compared to O₂ and air cases. On the other hand, more heterogeneous nucleation (as shown in figure S3) can occur because of the formation of fewer oxygen vacancies in air than under pure O₂, which

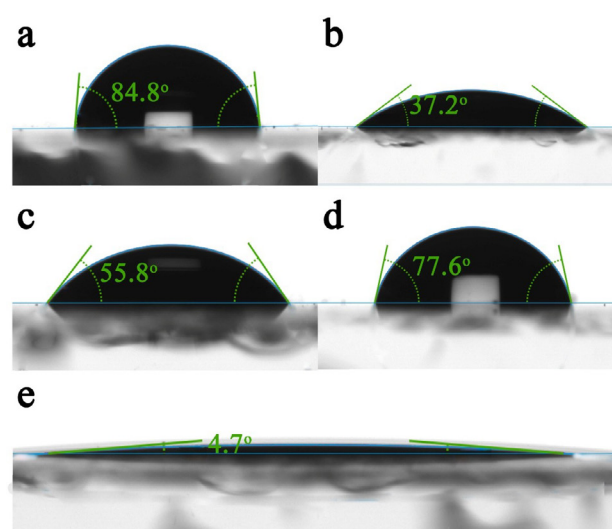


Figure 6. Wettability of MoO_x HTLs under different conditions, tested with water: a) untreated; (b) annealing in air at 300 °C, 120 min; (c) annealing in O₂ at 300 °C, 120 min; (d) annealing in N₂ at 300 °C, 120 min; (e) UV-ozone, 20 min.

induces a rougher surface compared with oxygen conditions and therefore the lowest contact angle. The variation of the contact angle was seemingly consistent with the performance of MoO_x in the PSCs, as indicated in figure 4. This could be understood by the correlation of the wettability of MoO_x and the grain morphology of perovskite. According to the literature, the wettability of DMF droplets is similar with water on the MoO_x surface [48]. A larger contact angle enables faster diffusion of the droplets and less drag force to the precursors so that less heterogeneous nucleation is induced. Moreover, as shown in figure 5(e), the UV-ozone treatment induces a very small contact angle, which could be a deteriorating factor for the formation of the perovskite layer in PSCs. Nevertheless, such a low contact angle could be beneficial for other devices such as gas sensors or photocatalytic devices based on MoO_x.

4. Conclusion

To summarize, we have fabricated the MoO_x material using a controllable electrochemical method and have systematically investigated its evolution of stoichiometry, morphology and

microstructure under different conditions (electrochemical parameters, annealing, chemical atmosphere, UV radiation, etc) for the first time. It can be seen that the oxygen vacancies can be effectively controlled by these conditions, to achieve the highest efficiency so far of 9.20%, and to influence the performance of MoO_x after integration into devices such as PSCs. Interestingly, the highest performance was obtained with the fewest oxygen vacancies by annealing under N₂ where the crystallization of MoO_x was not seemly very complete according to its characterization as well as its transparency. This suggests the dominant importance of the oxygen vacancy control in the application of MoO_x material. Further improvement is hopefully expected to enhance further understanding of the detailed mechanisms for future research. Furthermore, the variation of conditions has significantly influenced the wettability of the MoO_x film with the variation of the contact angle quite consistent with the results in corresponding solar cell performance, which has seemly been attributed to the cooperation of the oxygen vacancies and nucleation under different conditions. This work will hopefully provide ideas for other transition metal oxides such as NiO_x, CuO_x, etc, the photoelectric properties can be further improved by performing different post-treatments to achieve higher conversion efficiency of cells.

Acknowledgments

This work was supported by the National Natural Science Foundation of China (Grant Nos. 11834011, 11674225, 11474201 and 11204176).

ORCID iDs

Hong Liu  <https://orcid.org/0000-0002-2241-1199>

References

- [1] Park I J, Kang G, Park M A, Kim J S, Seo S W, Kim D H, Zhu K, Park T and Kim J Y 2017 *ChemSusChem* **10** 2660–7
- [2] Hsu C C, Su H W, Hou C H, Shyue J J and Tsai F Y 2015 *Nanotechnology* **26** 385201
- [3] Zuo C T and Ding L M 2015 *Small* **41** 5528–32
- [4] Soumyo C and Amlan J P 2016 *J. Phys. Chem. C* **120** 1428–37
- [5] Tseng Z L, Chen L C, Chiang C H, Chang S H, Chen C C and Wu C G 2016 *Sol. Energy* **139** 484–8
- [6] Xiao M D, Gao M, Huang F Z, Pascoe A R, Qin T S, Cheng Y B, Bach U and Spiccia L 2016 *ChemNanoMat* **2** 182–8
- [7] Chen C, Cheng Y, Dai Q L and Song H W 2015 *Sci. Rep.* **5** 17684
- [8] Li Y B et al 2016 *Nat. Commun.* **7** 12446
- [9] Thakur U K, Askar A M, Kisslinger R, Wiltshire B D, Kar P and Shankar K 2017 *Nanotechnology* **28** 274001
- [10] Meyer B J, Khalandovsky R, Görrn P and Kahn A 2010 *Adv. Mater.* **23** 70–3
- [11] Xu C, Cai P, Zhang X W, Zhang Z L, Xue X G, Xiong J and Zhang J 2017 *Sol. Energy Mater. Sol. Cells* **159** 136–42
- [12] Dasgupta B, Ren Y, Wong L M, Kong L Y, Tok E S, Chim W K and Chiam S Y 2015 *J. Phys. Chem. C* **119** 10592–601
- [13] Rouhani M, Foo Y L, Hobley J, Pan J, Subramanian G S, Yu X J, Rusydi A and Gorelik S 2013 *Appl. Surf. Sci.* **273** 150–8
- [14] Rouhani M, Hobley J, Subramanian G S, Phang I Y, Foo Y L and Gorelik S 2014 *Sol. Energy Mater. Sol. Cells* **126** 26–35
- [15] Wang S F, Fan W R, Liu Z C, Yu A B and Jiang X C 2018 *J. Mater. Chem. C* **6** 191–212
- [16] Gavriluk A, Tritthart U and Gey W 2011 *Sol. Energy Mater. Sol. Cells* **95** 1846–51
- [17] Rahmani M B, Keshmiri S H, Yu J, Sadek A Z, Al-Mashat L, Moafi A, Latham K, Li Y X, Wlodarski W and Kalantar-Zadeh K 2010 *Sensors Actuators B* **145** 13–9
- [18] Manal M Y A A, Matthew R F, Billy J M, Torben D, Kay L, Adam F C, Ahmad S Z, Salvy P R, Jian Z O and Kourosh K 2014 *Nanoscale* **6** 12780–91
- [19] Illyaskutty N, Sreedhar S, Sanal K G, Kohler H, Schwotzer M, Natzeck C and Mahadevan Pillai V P 2014 *Nanoscale* **6** 13882–94
- [20] Rathnasamy R and Alagan V 2018 *Physica E* **102** 146–52
- [21] Wu D, Shen R, Yang R, Ji W X, Jiang M, Ding W P and Peng L M 2017 *Sci. Rep.* **3** 44697
- [22] Wang F X, Qiao X F, Xiong T and Ma D G 2008 *Org. Electron.* **9** 985–93
- [23] Werner J, Geissbühler J, Dabirian A, Nicolay S, Masis M M, Wolf S D, Niesen B and Ballif C 2016 *ACS Appl. Mater. Interfaces* **8** 17260–7
- [24] Ganchev M, Sendova-Vassileva M, Popkirov G and Vitanov P 2016 *J. Phys.: Conf. Ser.* **764** 012011
- [25] Cauduro A L F, dos Reis R, Chen G, Schmid A K, Méthivier C, Rubahn H G, Bossard-Giannesini L, Cruguel H, Witkowski N and Madsen M 2017 *ACS Appl. Mater. Interfaces* **9** 7717–24
- [26] Lee K E, Liu L J and Kelly T L 2014 *J. Phys. Chem. C* **118** 27735–41
- [27] Kao P C, Chen Z H, Yen H E, Liu T H and Huang C L 2018 *Japan. J. Appl. Phys.* **57** 03DA04
- [28] Han B C, Gao M, Wan Y Z, Li Y, Song W L and Ma Z Q 2018 *Mater. Sci. Semicond. Process.* **75** 166–72
- [29] Yang T, Wang M, Cao Y, Huang F, Huang L, Peng J, Gong X, Cheng S Z D and Cao Y 2012 *Adv. Energy Mater.* **2** 523–7
- [30] Patil P R and Patil P S 2001 *Thin Solid Films* **382** 13–22
- [31] Gacitua M et al 2010 *Phys. Status Solidi a* **8** 1905–11
- [32] Upadhyay K K, Nguyen T, Silva T M, Carmezim M J and Fatima Montemor M 2016 *Electrochim. Acta* **225** 19–28
- [33] Yao D D, Ou J Z, Latham K, Zhuikov S, O'Mullane A P and Kalantar-zadeh K 2012 *Cryst. Growth Des.* **12** 1865–70
- [34] Petrova M L, Bojinov M S and Gadjev I H 2011 *Bulg. Chem. Commun.* **43** 60–3
- [35] Zhou F, Liu H, Wang X W and Shen W Z 2017 *Adv. Funct. Mater.* **27** 1606156
- [36] Jeon Y, Kim S, Yim S and Yim S 2013 *J. Nanoelectron. Optoelectron.* **8** 584–7
- [37] Huang J S, Lee C Y and Chin T S 2013 *Electrochim. Acta* **91** 62–8
- [38] Agarwala P and Kabra D 2017 *J. Mater. Chem. A* **5** 1348
- [39] Naumkin A V, Kraut-Vass A, Gaarenstroom S W and Powell C J 2000 NIST X-ray Photoelectron Spectroscopy Database (<https://doi.org/10.18434/T4T88K>)

- [40] Choi J G and Thompson L T 1996 *Appl. Surf. Sci.* **93** 143–9
- [41] Guo Y X, Yin X T, Liu J, Chen W, Wen S, Que M D, Tian Y P, Yang Y W and Que W X 2018 *J. Adv. Dielectr.* **8** 1850006
- [42] Güntner A T, Righettoni M and Pratsinis S E 2016 *Sensors Actuators B* **223** 266–73
- [43] Xiong J, He Z, Zhan S P, Yang B C, Zhang X W, Cai P, Xu C, Xue X G and Zhang J 2017 *Curr. Appl. Phys.* **17** 1021–8
- [44] Vasilopoulou M et al 2012 *J. Am. Chem. Soc.* **134** 16178–87
- [45] Gómez E, Pellicer E and Vallés E 2005 *J. Electroanal. Chem.* **580** 238–44
- [46] Dos Santos S, Poulikakos L D and Partl M N 2017 *Int. J. Pavement. Res. Technol.* **10** 2–14
- [47] Bhusan B, Luo D, Schricker S R, Sigmund W and Zauscher S 2014 *Handbook of Nanomaterial Properties* (Berlin: Springer) p 899
- [48] Zhou Y Q, Wu B S, Lin G H, Xing Z, Li S H, Deng L L, Chen D C, Yun D Q and Xie S Y 2018 *Adv. Energy Mater.* **8** 1800399